J. Phys.: Condens. Matter **24** (2012) 275501 (14pp) doi:10.1088/0953-8984/24/27/275501

Thermoelectric transport in strained Si and Si/Ge heterostructures

N F Hinsche[1], **I Mertig**[1,2] **and P Zahn**[1,3]

[1] Institut für Physik, Martin-Luther-Universität Halle-Wittenberg, D-06099 Halle, Germany
[2] Max-Planck-Institut für Mikrostrukturphysik, Weinberg 2, D-06120 Halle, Germany
[3] Helmholtz-Zentrum Dresden-Rossendorf, PO Box 51 01 19, D-01314 Dresden, Germany

E-mail: nicki.hinsche@physik.uni-halle.de

Received 23 April 2012, in final form 23 May 2012
Published 19 June 2012
Online at stacks.iop.org/JPhysCM/24/275501

Abstract
The anisotropic thermoelectric transport properties of bulk silicon strained in the [111]-direction were studied by detailed first-principles calculations focusing on a possible enhancement of the power factor. Electron and hole doping were examined in a broad doping and temperature range. At low temperature and low doping an enhancement of the power factor was obtained for compressive and tensile strain in the electron-doped case and for compressive strain in the hole-doped case. For the thermoelectrically more important high-temperature and high-doping regime a slight enhancement of the power factor was only found under small compressive strain with the power factor overall being robust against applied strain. To extend our findings the anisotropic thermoelectric transport of a [111]-oriented Si/Ge superlattice was investigated. Here, the cross-plane power factor under hole doping was drastically suppressed due to quantum-well effects, while under electron doping an enhanced power factor was found. For this, we state figures of merit of $ZT = 0.2$ and 1.4 at $T = 300$ and 900 K for the electron-doped [111]-oriented Si/Ge superlattice. All results are discussed in terms of band structure features.

(Some figures may appear in colour only in the online journal)

1. Introduction

Thermoelectric phenomena were first described for metals by Seebeck at the beginning of the 19th century and revived by Ioffe in the late 1950s by the introduction of semiconductors to thermoelectric devices [1, 2]. However, since then thermoelectrics have been restricted to a scientific and economic niche mainly due to their poor conversion efficiency [3, 4]. Nowadays the emerging global need for energy production and conservation has intensified interest and research in more effective alternative energy technologies to reduce our dependence on fossil fuels. Contributing to this, thermoelectric devices could partially convert wasted heat into electricity by their ability to transform heat directly into electric current, and vice versa [5].

The thermoelectric conversion efficiency can be stated by the figure of merit (FOM)

$$ZT = \frac{\sigma S^2}{\kappa_{\mathrm{el}} + \kappa_{\mathrm{ph}}} T, \tag{1}$$

where σ is the electrical conductivity, S is the thermopower, κ_{el} and κ_{ph} are the electronic and phononic contributions to the thermal conductivity, respectively. The numerator of equation (1) is called the power factor $\mathrm{PF} = \sigma S^2$ and characterizes the electric power output.

While thermoelectric devices are extremely facile, have no moving parts, and do not produce greenhouse gases [6], two obstacles limit their applicability. The first, a low efficiency, could be challenged by the nanostructured thermoelectrics of today enabling large values of $ZT \gg 1$ [7–9]. As a second drawback, the materials are based on environmentally hazardous or rare lead, tellurium or selenium compounds and are therefore hard to integrate in semiconductor electronics.

However, current research has achieved tremendous progress in enabling silicon for thermoelectrics. Silicon is non-toxic, readily available, cheap and well integrated in the present electronics infrastructure, so this might be a considerable leap forward. While silicon has been stated as an inefficient thermoelectric in the past due to its enormous

thermal conductivity [10], recent experimental and theoretical attempts have revealed that nanostructuring could lead to thermoelectric efficiencies comparable to state-of-the-art commercial thermoelectric materials [11–14].

Besides the reduction of thermal conductivity, that is the denominator in equation (1), Koga *et al* showed in a seminal work [15, 16] that it should be possible to enhance the power factor, that is the numerator in equation (1). This concept of carrier pocket engineering uses the influence of strain to optimize the band structure of silicon and germanium based superlattices (SLs) regarding their electronic transport. As a main result it was found that the effect of the lattice strain at the Si/Ge interfaces is more relevant for strain in the [111]-direction than in the [001]-direction with respect to a possible enhancement of the power factor. In fact, $ZT = 1.25$ and $ZT = 0.98$ at room temperature were predicted for strain-non-symmetrized and strain-symmetrized [111]-oriented Si/Ge-SLs, respectively, and the ZT values are shown to increase significantly at elevated temperatures [17].

While in a previous study we have already concentrated on the influence of biaxial in-plane strain in the [001]-direction on the thermoelectric properties of silicon [18], we will focus here on the influence of strain along the [111]-direction. For this purpose the paper is organized as follows. In section 2 we introduce our approach based on first principle electronic structure calculations within density functional theory and transport calculations based on the solution of the linearized Boltzmann equation. By this means we start the discussion of the thermoelectric transport properties of bulk silicon strained along the [111]-direction in dependence on the strain and doping to gain insight into the physical mechanisms, which clearly differ from the [001]-strain case. A discussion is given for electron as well as for hole doping in sections 3.1 and 3.2, respectively.

To extend the findings for strained bulk silicon, in section 3.3 results for an exemplary Si/Ge-SL grown on Si in the [111]-direction are presented. Here the influence of tensile strain in the [111]-direction, induced by the lattice mismatch at the Si/Ge interface, is investigated with respect to the thermoelectric transport in-plane and cross-plane in the SL. Again, the temperature and doping dependences of the thermoelectric properties are discussed for electron and hole doping regarding a possible enhancement of the power factor. A further aspect will be the influence of structural relaxation and chemical composition on the transport properties. At the end of the paper, in section 3.4 insights into the FOM will be presented along with the electronic part of the thermal conductivity, to give a clue on optimal charge carrier concentrations to obtain the best FOM.

While focusing our interest on the high-temperature thermoelectric application of strained silicon, our results in the room-temperature regime could be of importance for the metal–oxide–semiconductor device community. Knowledge of the thermoelectric properties of silicon under strain could help in understanding parasitic effects on the electronic transport in those structures. In this low-temperature and low-doping regime we confirm a remarkable influence of externally applied strain on the electrical transport under electron and hole doping.

2. Methodology

Our approach is based on two constituents: first-principles density functional theory calculations (DFT), as implemented in the QuantumEspresso package [19] and an in-house developed Boltzmann transport code [18, 20–22] to calculate the thermoelectric properties.

First, the band structure of the strained and unstrained Si was calculated using the general gradient approximation (GGA) with the Perdew–Burke–Ernzerhof (PBE) flavour of exchange correlation functional [23]. Fully relativistic and norm-conserving pseudopotentials [24] were used to treat the spin–orbit splitting of the Si valence bands appropriately. The calculations for the bulk Si were performed with the rhombohedral experimental lattice constant $a_0 = 5.434\ \text{Å}/\sqrt{2}$ for a rhombohedral two atom unit cell, which is sketched in the inset of figure 1(c). The strain in the [111]-direction under constant volume is simulated by changing the lattice constant a and the angle α_r. Throughout the paper the biaxial strain will be given in units of the relative change of the in-plane lattice constant, that is the nearest neighbour distance in the [111]-plane as $\Delta a = a_{[111]}$ or $a_\parallel/a_0$ following the notation of previous works [18, 21, 25, 26]. The angle α_r is given by $\cos\alpha_r = 1 - \frac{3(1+\Delta a/a_0)^6}{4+2(1+\Delta a/a_0)^6}$. That means that tensile in-plane strain considers changes ${}^{\Delta a}/_{a_0} > 0$ and $\alpha_r > 60°$, while compressive in-plane strain means ${}^{\Delta a}/_{a_0} < 0$ and $\alpha_r < 60°$. As used previously in the literature, tensile strain along the [111]-direction coincides with compressive in-plane strain as denoted here.

By this trigonal deformation an atomic relaxation of the atomic positions inside the unit cell is possible, as the displacement of the two sublattices along the [111]-direction is no longer given by symmetry. To obtain the atomic positions of the strained silicon we performed structural relaxations using VASP [27]. The atomic positions were optimized such that the Hellmann–Feynman forces on them were below 0.1 meV Å^{-1}. At the same time the given deformed lattice parameters were not allowed to relax and conservation of the unit cell volume was assumed. A volume relaxation at the maximum strain ${}^{\Delta a}/_{a_0} \pm 1\%$ resulted in a volume reduction by 0.2% which corresponds to a lattice constant change by less than 0.1%.

As expected, our DFT calculations underestimate the size of the bandgap at zero temperature and do not reproduce the temperature dependence of the gap. For this purpose we implemented a temperature-dependent scissor operator [28], so that the strain- and temperature-dependent energy gap E_g becomes

$$E_g\left(T, \frac{\Delta a}{a_0}\right) = E_g\left(T = 0, \frac{\Delta a}{a_0}\right) + U_{GGA} - \frac{\alpha T^2}{T + \beta}, \quad (2)$$

where $E_g(T = 0, \frac{\Delta a}{a_0})$ is the zero temperature gap obtained by our self-consistent DFT calculations, $U_{GGA} = 0.57$ eV is a static correction to reproduce the experimental low-temperature gap and the third part of equation (2) is the correction of the temperature dependence of the bandgap in a wide temperature range [29], with $\alpha = 4.73 \times 10^{-4}$ eV K^{-1}, T the absolute temperature and $\beta = 636$ K for bulk silicon.

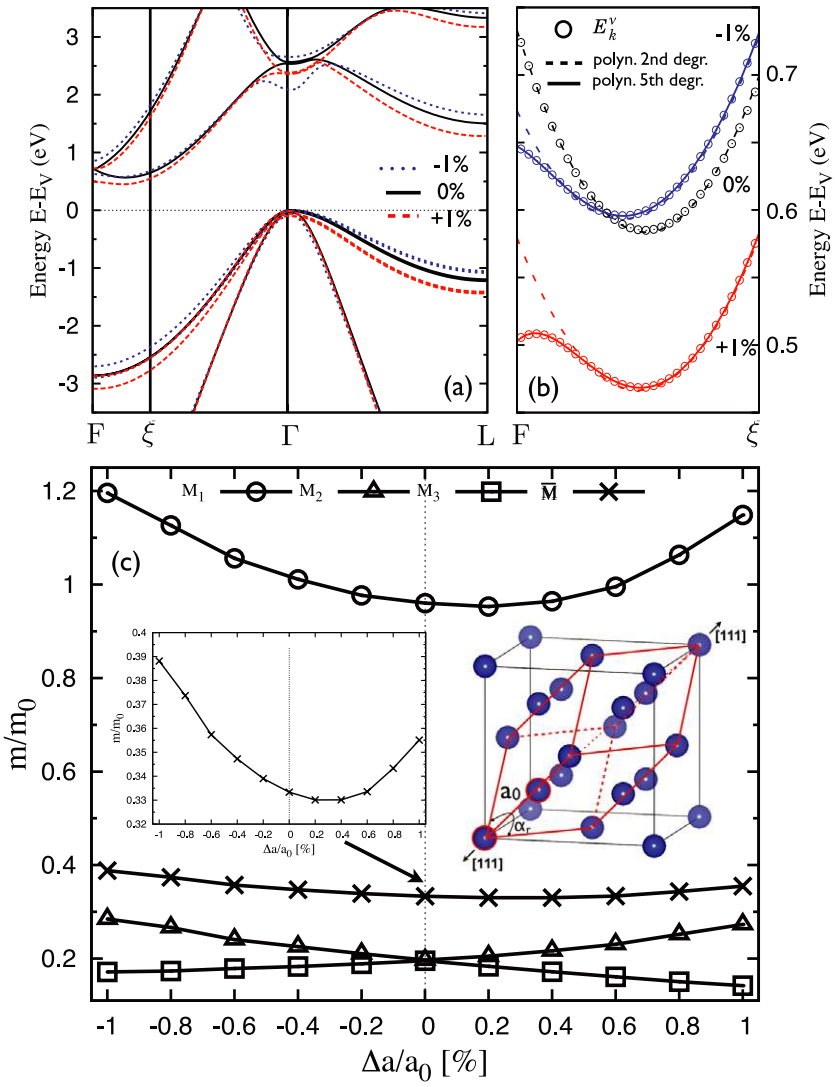

Figure 1. The band structure of bulk silicon in the rhombohedral unit cell. In the unstrained case, the F point coincides with the X point of the fcc Brillouin zone. (a) The bands for the unstrained case (black solid line), under 1% compressive strain (blue dotted line) and under 1% tensile strain (red dashed line) are shown. In (b) a zoom near the conduction band minimum elucidates the nonparabolicity of the bands under applied strain. (c) Directional effective conduction band masses for silicon under [111]-strain. The insets show in detail the response of the averaged effective mass $\bar{M}$ on the applied strain, as well as the rhombohedral unit cell [41] (red lines). More details are given in the text.

Converged results from the first step are the basis to obtain the thermoelectric transport properties by solving the linearized Boltzmann equation in the relaxation time approximation (RTA) [20]. Boltzmann transport calculations for thermoelectrics have been carried out for quite a long time and show reliable results for metals [30, 31] as well as for wide- and narrow-gap semiconductors [18, 21, 32, 33] in the diffusive limit of transport. Here the relaxation time is assumed to be constant with respect to the wavevector k and energy on the scale of $k_B T$. The constant relaxation time allows for the calculation of the thermopower S without any free parameters. To reproduce experimental findings we parametrized the doping-dependent relaxation times from mobility measurements on unstrained silicon according to [34] by

$$\tau(N) = ((-c/\pi \arctan[a \lg(N/N_0)] + c/2) + 2\lg(N/N_1)^2)d, \quad (3)$$

with $a = 1.8, N_0 = 10^{17}$ cm$^{-3}, N_1 = 10^{17.5}$ cm$^{-3}, c = 1500, d = 0.15$ fs ($a = 1.3, N_0 = 10^{16.8}$ cm$^{-3}, N_1 = 10^{17.5}$ cm$^{-3}, c = 550, d = 0.13$ fs) for electron (hole) doping and charge carrier concentrations of N between 10^{14} and 10^{22} cm^{-3}. Nevertheless, we state that our relaxation time is not strain-dependent, while it is known that under strain the dominant scattering process alters: for unstrained Si, the room-temperature scattering is dominated by optical phonons, i.e., intervalley scattering, whereas for strained Si, the scattering by optical phonons is reduced [35, 36].

With the transport distribution function (TDF) as termed by Mahan and Sofo [37]

$$\mathcal{L}^{(n)}_{\perp,\parallel}(\mu, T) = \frac{\tau}{(2\pi)^3} \sum_v \int \mathrm{d}^3\mathbf{k} \, (v^v_{\mathbf{k},(\perp,\parallel)})^2 \times (E^v_{\mathbf{k}} - \mu)^n \left(-\frac{\partial f_{(\mu,T)}}{\partial E}\right)_{E=E^v_{\mathbf{k}}} \quad (4)$$

the temperature- and doping-dependent electrical conductivity σ and thermopower S are defined as

$$\sigma_{\perp,\parallel} = e^2 \mathcal{L}^{(0)}_{\perp,\parallel}(\mu, T), \qquad S_{\perp,\parallel} = \frac{1}{eT} \frac{\mathcal{L}^{(1)}_{\perp,\parallel}(\mu, T)}{\mathcal{L}^{(0)}_{\perp,\parallel}(\mu, T)}. \quad (5)$$

Here $\parallel$ denotes the in-plane direction parallel to the a-axis and $\perp$ the cross-plane direction. The electronic part of the total thermal conductivity amounts to

$$\kappa_{\mathrm{el}\perp,\parallel} = \frac{1}{T}\left(\mathcal{L}^{(2)}_{\perp,\parallel}(\mu, T) - \frac{(\mathcal{L}^{(1)}_{\perp,\parallel}(\mu, T))^2}{\mathcal{L}^{(0)}_{\perp,\parallel}(\mu, T)}\right). \quad (6)$$

$E^{\nu}_{\mathbf{k}}$ denotes the band structure of band ν, $v^{\nu}_{\mathbf{k}}$ the group velocity and $f_{(\mu,T)}$ the Fermi–Dirac-distribution with chemical potential μ. The chemical potential μ at temperature T and extrinsic carrier concentration N is determined by an integration over the density of states $n(E)$,

$$N = \int_{\mu-\Delta E}^{\mathrm{VBM}} \mathrm{d}E\, n(E)[f_{(\mu,T)} - 1] + \int_{\mathrm{CBM}}^{\mu+\Delta E} \mathrm{d}E\, n(E) f_{(\mu,T)}, \quad (7)$$

where CBM is the conduction band minimum and VBM is the valence band maximum. The necessary size of ΔE will be discussed below.

In a recent work we showed that the determination of surface integrals in anisotropic Brillouin zones is demanding with respect to convergence of the transport property anisotropy [22]. Therefore the constant energy-surface integrations, which are required in equation (4), are performed within an extended tetrahedron method [38–40] interpolating the calculated eigenvalues $E^{\nu}_{\mathbf{k}}$ on an adaptive **k**-mesh corresponding to a density of at least 44 000 **k** points in the irreducible part of the Brillouin zone. $\mathcal{L}^{(0)}_{\perp,\parallel}(E, T = 0)$ was determined on a dense energy mesh with a step width of 1 meV. At vanishing strain $^{\Delta a}/_{a_0} = 0$ the numerical errors of $\sigma_{\parallel}/\sigma_{\perp}$ and $S_{\parallel}/S_{\perp}$ were constantly below 0.1%. In the limit of low carrier concentrations $N \leq 1 \times 10^{14}$ cm^{-3} and for larger carrier concentrations in the bipolar conduction regimes at high temperatures, convergence of the integrals (4) and (7) was achieved with an adaptive integration method for ΔE of at least $10 k_{\mathrm{B}} T$.

3. Thermoelectric transport

3.1. [111]-strained silicon: electron doping

In figure 1(a) the uncorrected band structure of bulk silicon in the rhombohedral unit cell is shown for the unstrained case (black solid line), under 1% tensile strain (red dashed line) and for −1% compressive strain (blue-dotted line) on relevant high symmetry lines. Unstrained silicon has an indirect bandgap with conduction band minimum (CBM) near the F high symmetry point. The CBM consists of sixfold degenerate (Δ_6) prolate spheroidal isoenergetic surfaces along six equivalent Γ–F directions. Due to symmetry of the lattice distortion in the [111]-direction this degeneracy holds under applied strain in contrast to strain applied along the [001]-direction [18].

In the unstrained case, for each Δ_6-valley the effective masses along the major and the minor axis are $M_1 = 0.91 m_0$ and $M_2 = 0.19 m_0$, respectively. As can be seen from figure 1(b) the idea of an effective mass determined by a second order polynomial fit (dashed lines in figure 1(b)) is valid for the unstrained case, but band warping leads to deviations for silicon under strain already for small band occupations. Here, a fifth order polynomial fit (solid lines in figure 1(b)) is necessary to reproduce the band dispersion, which occurs under applied biaxial [111]-strain. It is therefore advisable to go beyond a simplified effective mass model. In contrast to the conduction bands, the [111]-strain leads to a splitting of the degenerate valence bands, the heavy-hole (HH) and light-hole (LH) bands, similarly to the case of [001]-strain [18, 42]. While the spin–orbit-split-off band is 40 meV away from the band edge, the HH band lifts up energetically under tensile strain, while the LH band lowers in energy. This picture reverses under opposite strain conditions [43]. While the indirect gap closes linearly under tensile in-plane strain from 0.58 eV in equilibrium to about 0.45 eV at $^{\Delta a}/_{a_0} = 1\%$, the gap size is almost constant within 0.01 eV under compressive strain within the considered range [26, 44, 45] (cf figure 1(b)). The direct gap at Γ decreases slightly under applied strain, in a more pronounced way under compressive in-plane strain.

The influence of biaxial in-plane strain on the fitted effective masses is summarized in figure 1(c). The change of the effective mass M_1 along the major axis is almost symmetric to the applied strain and increases up to 130% of the unstrained value. In contrast, the transverse effective masses behave drastically differently. While the transverse effective mass M_2 increases under tensile strain, the effective mass M_3 perpendicular to M_2 decreases. This behaviour is reversed under applied compressive strain. These results are in good agreement with other findings [44, 45], but add up to GW calculations where only one transverse mass with an almost constant value was found [26]. The strain-dependent averaged effective mass $\bar{M} = \prod_{i=1}^{3} (M_i)^{1/3}$, often referred to as the density-of-states effective mass, is shown additionally as an inset in figure 1(c).

In the following the influence of trigonal distortion on the thermoelectric transport of Si under electron doping will be discussed. For this purpose two doping and temperature regimes are considered. The first, at a low temperature of $T = 100$ K and low charge carrier concentration of $N = 1 \times 10^{15}$ cm^{-3}, is suitable for metal–oxide–semiconductor device applications. The results for the electrical conductivity, thermopower and power factor in dependence on the in-plane strain are shown in figures 2(a)–(c), respectively. Under tensile strain the in-plane electrical conductivity $\sigma_{\parallel}$ increases almost linearly, while the cross-plane component $\sigma_{\perp}$ decreases almost comparably. For compressive strain the behaviour reverses, with the cross-plane conductivity being enhanced up to 23% at 1% compressive strain, while the in-plane conductivity decreases to nearly 23% of the unstrained value under 1% tensile strain. In the limit of a degenerate semiconductor at low temperatures and small charge carrier concentrations these results can be completely

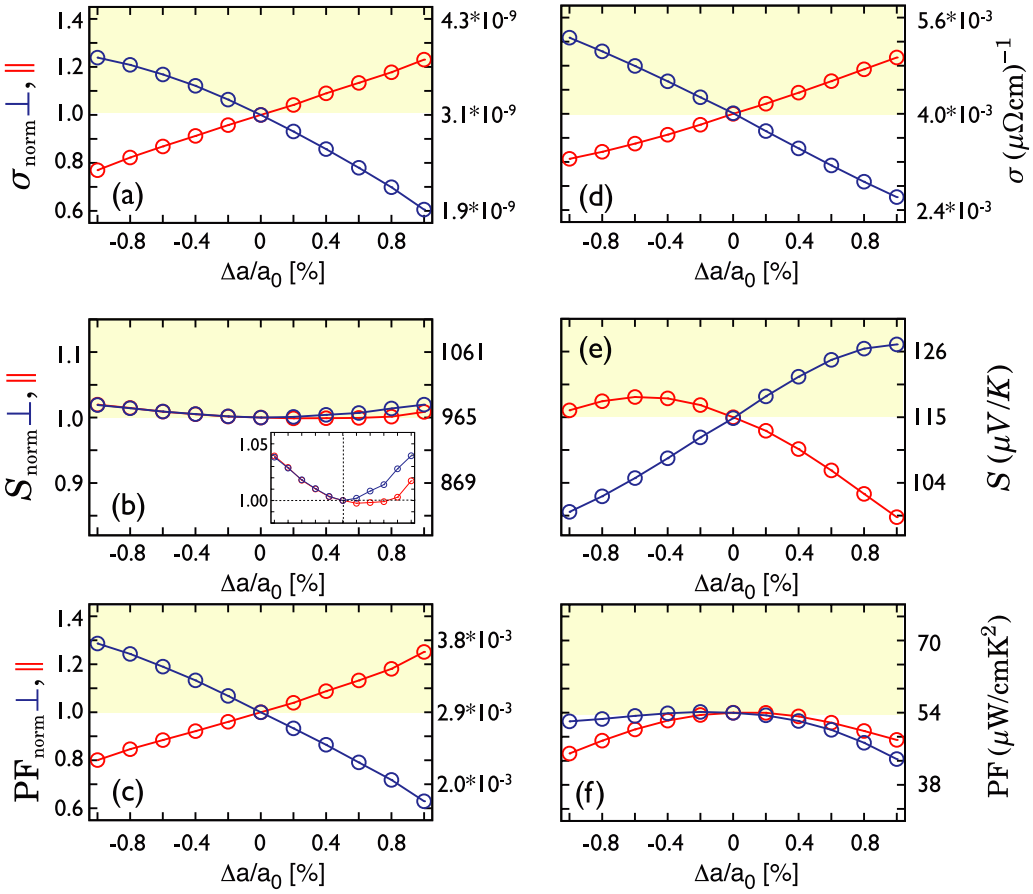

Figure 2. The anisotropic thermoelectric transport properties of Si for fixed temperature and electron doping concentrations in dependence on the compressive and tensile strain in the [111]-direction. The left panels ((a)–(c)) correspond to an electron doping of 2×10^{-8} e/atom ($N = 1 \times 10^{15}$ cm^{-3}) at a temperature of 100 K, while the right panels ((d)–(f)) refer to an electron doping of 0.04 e/atom ($N = 2 \times 10^{21}$ cm^{-3}) at a temperature of 900 K. On the left axis of each figure the relative value compared to the unstrained case is shown, while on the right axis the absolute values are given.

understood within an effective mass calculation [22]. With noticeable variation of the electrical conductivity under applied strain, the thermopower is almost unaffected. At low temperatures only a small energy window near the band edges plays an important role for the determination of the thermopower. As the functional change of the coefficients $\mathcal{L}_{\perp,\parallel}^{(0,1)}(\mu, T)$ is determined by parabolic bands and a strain-dependent shift of the chemical potential, a strong change in the thermopower cannot be expected. However, a slight upward tendency for the thermopower under compressive and tensile strain can be stated. As $S \propto (E_{\mathrm{CBM/VBM}} - \mu)^{-1} \propto \bar{M}$, this can be directly linked to the strain dependence of $\bar{M}$ (cf figure 1(c)). For tensile strain an anisotropy of the thermopower is apparent, which seems to be suppressed for compressive strain. This could be linked to stronger deviations from the isotropic effective mass for tensile strain as shown in figure 1(b).

The strain dependence of the resulting power factor PF is shown in figure 2(c). Due to the weak impact of the thermopower, the behaviour of the power factor is dominated by the electrical conductivity dependence on the applied strain. At low temperatures and small charge carrier concentrations, such a behaviour has already been observed for biaxially strained silicon [18]. However, the additional power output described by the power factor is enhanced by 30% under 1% applied compressive strain for $PF_{\perp}$ and by 25% under 1% applied tensile strain for $PF_{\parallel}$. We note that this low temperature and small doping case is not feasible for thermoelectric power generation, but could give insight into the parasitic effects which play a role in metal–oxide–semiconductor devices.

The usual conditions for silicon-based thermoelectric applications, such as a high temperature of 900 K and large charge carrier concentrations $N = 2 \times 10^{21}$ cm^{-3} are assumed in figures 2(d)–(f). At a temperature of 900 K the electronic band structure on a width $\pm\Delta E = \pm 800$ meV around the position of the chemical potential has to be considered, which makes a simplified description of the electronic transport properties within a spherical band picture inaccurate. However, the dependence of the electrical conductivity (cf figure 2(d)) on the applied [111]-strain is almost preserved, even if accidentally. This is in contrast to biaxial strain in the [001]-direction, where the strain dependence induced by reoccupation of bands is suppressed under higher temperatures and dopings [18, 35].

In figure 2(e) the anisotropic thermopower under trigonal distortion is shown. The cross-plane thermopower shows a monotonic increase from 85% to 110% of the unstrained

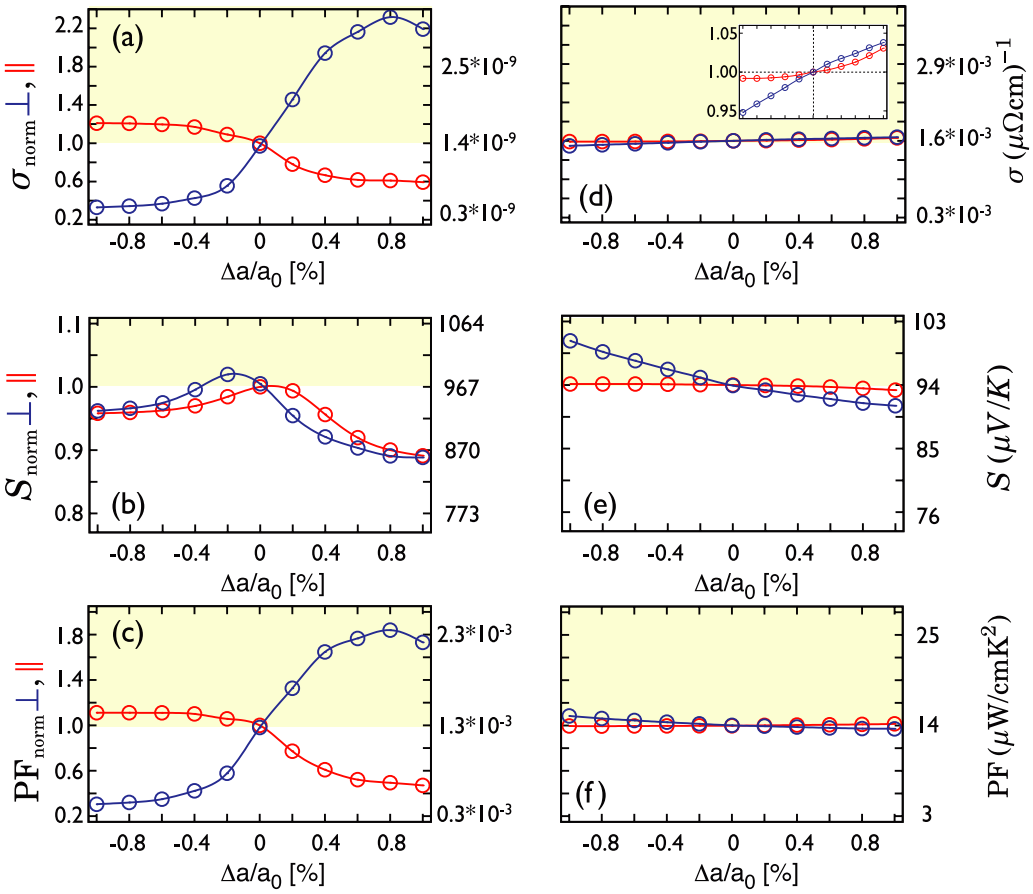

Figure 3. The anisotropic thermoelectric transport properties of Si for fixed temperature and hole doping concentrations in dependence on the compressive and tensile strain in the [111]-direction. The left panels ((a)–(c)) correspond to a hole doping of 2×10^{-8} e/atom ($N = 1 \times 10^{15}$ cm^{-3}) at a temperature of 100 K, while the right panels ((d)–(f)) refer to a hole doping of 0.04 e/atom ($N = 2 \times 10^{21}$ cm^{-3}) at a temperature of 900 K. On the left axis of each figure the relative value compared to the unstrained case is shown, while on the right axis the absolute values are given.

thermopower value of $S_\perp = 115$ μV K^{-1} varying from compressive to tensile strain. The in-plane component $S_\parallel$ decreases to 85% of the unstrained thermopower value under 1% tensile strain. A very similar behaviour was found for the thermopower of biaxially strained silicon in the [001]-direction [18]. The compensation effects of the enhanced thermopower and decreased electrical conductivity, and vice versa, are well known for thermoelectrics under strain [18, 21, 46]. This scenario holds for [111]-strained silicon, too. In figure 2(f) the anisotropic power factor shown in the in-plane and cross-plane directions is always smaller than the power factor of the undistorted system, with $PF_\perp$ being at least stable under small values of compressive strain. We mention that the absolute values (cf the right scales in figures 2(a) and (d)) of the electrical conductivity are increased remarkably compared to the low-doping case as expected. Due to this, the absolute value of the power factor increases its absolute value, but unfortunately does not show an enhancement due to mechanical strain in the [111]-direction. Furthermore, compared to the low-doping/low-temperature regime (figure 2(c)) the power factor does not show noticeable anisotropy between the in-plane and cross-plane components.

3.2. [111]-strained silicon: hole doping

As is well known, thermoelectric devices use two types of semiconductor, namely n-type and p-type, which are connected in series [6]. Therefore, the influence of biaxial [111]-strain on hole-doped silicon is presented in figure 3 in the same way as was done for the electron-doped case. In the low-doping/low-temperature regime an enormous enhancement for the cross-plane electrical conductivity $\sigma_\perp$ under sufficient tensile strain can be found (cf figure 3(a)), while the in-plane component $\sigma_\parallel$ decreases more slightly under the same strain conditions. This behaviour can be linked to a changed subband structure. As mentioned before, strain lifts the degeneracy of the LH and HH bands around the Γ point and alters the curvature, that is the effective mass, of both bands. Under applied strain, the valence bands become highly anisotropic and a crossover between bands occurs so that they even lose their original LH and HH meanings [18, 25]. Extended discussions on this can be found in [43, 47].

The thermopower of p-type silicon is shown in figure 3(b). The thermopower in-plane and cross-plane decreases slightly under tensile as well as under compressive strain. The anisotropy of the thermopower is moderate. As previously reported [18, 48], the thermopower depends

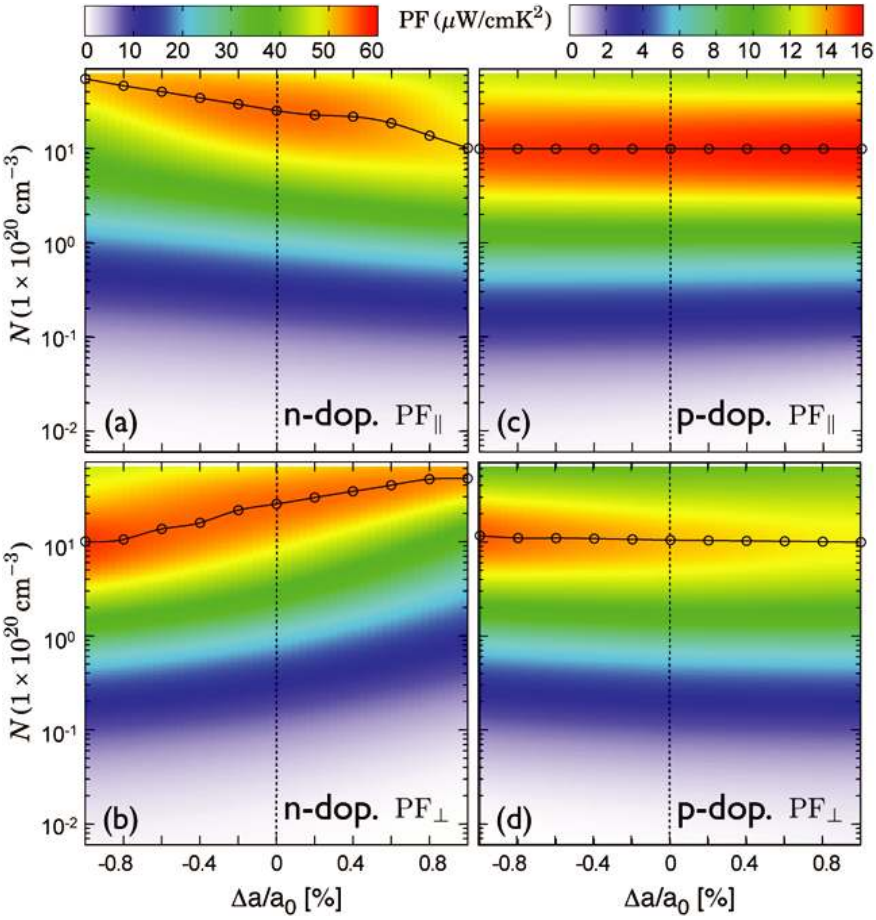

Figure 4. In-plane and cross-plane power factor of Si at a fixed temperature of 900 K under electron ((a), (b)) and hole doping ((c), (d)) for varying charge carrier concentration and applied [111]-strain. The black circles emphasize the position of optimal doping at a certain strain state to maximize the power factor. Note the different scales for electron and hole doping.

strongly on the number of occupied carrier pockets. A higher valley degeneracy at a fixed charge carrier concentration leads to an increased thermopower. As already mentioned, the formerly degenerate HH and LH bands split under tensile and compressive strain. At low hole concentrations and low temperatures only the former HH (LH) band is occupied. This leads directly to a reduction of $S_\parallel$ and $S_\perp$. Consequently, the accompanied power factor (cf figure 3(c)) is also reduced in its maximal possible enhancement, but follows in principle the behaviour given by the electrical conductivity.

For high temperatures and high hole concentrations the results are shown in figures 3(d)–(f). As the carrier concentration is raised by nearly six orders of magnitude with respect to the low-doping case, the absolute value of the electrical conductivity increases in the same order (note the right scale of figure 3(d)). Unfortunately, due to the higher band occupation and the broader smearing of the Fermi–Dirac-distribution, the effects of redistribution in strain-split bands do not play a role any more. Moreover, the effects of reduced and increased effective masses cancel each other leading to negligible change, in absolute values as well as in anisotropy, of the hole electrical conductivity.

For the hole thermopower shown in figure 3(e) this behaviour is still valid. For the in-plane thermopower $S_\parallel$ no significant influence of either compressive or tensile strain could be found. A minor dependence on applied [111]-strain is observed for $S_\perp$. Here, the cross-plane thermopower decreases from 100 to 91 μV K^{-1} for strain values varying from 1% compressive to 1% tensile strain.

Comprising the results for the electrical conductivity and thermopower, the resulting power factor under hole doping is shown in figure 3(f). No evident influence of [111]-strain on the power factor could be found in the thermoelectrically relevant temperature and hole doping regime. Furthermore, the absolute value of the power factor is about 3–4 times smaller than in the comparable electron-doped case, which is mainly caused by the higher hole scattering rate as assumed in equation (3). At varying strain not only do the absolute values of the thermoelectric properties change, but also the optimal charge carrier concentrations to obtain these maximized values. For biaxially [001]-strained silicon it was found that the optimal doping range can change by a factor of two, while reducing the power factor by up to 20% if not adapting the charge carrier concentration [18]. Therefore, the in-plane and cross-plane power factor under varying electron and hole doping, as well as varying [111]-strain is shown in figure 4. The maximized power factor at optimal charge carrier concentration at a given strain state is emphasized by a

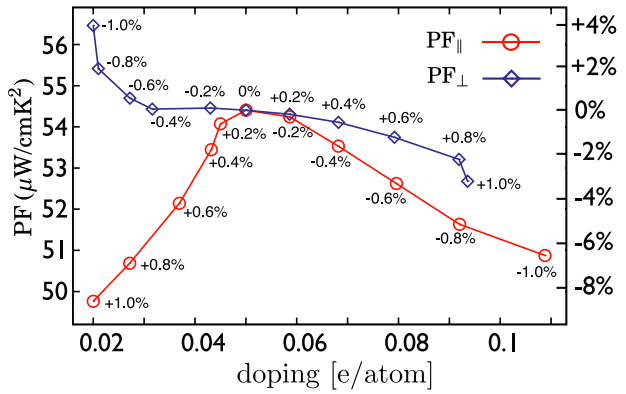

Figure 5. Maximized in-plane and cross-plane power factors of [111]-strained Si at a fixed temperature of 900 K under optimal electron doping. The figure highlights the path of the black circles in figures 4(a) and (b). $N = 0.01$ e/atom corresponds to $N = 5 \times 10^{20}$ cm^{-3}.

black-dotted line in figures 4(a)–(d). Comparing silicon under electron doping (cf figures 4(a) and (b)) and hole doping (cf figures 4(c) and (d)), it is obvious that electron-doped silicon shows a much stronger variation of the optimal doping range. For the in-plane component $PF_{\parallel}$ and electron doping the optimal carrier concentration decreases by about a factor of 5, from $N = 5 \times 10^{21}$ to 1×10^{21} cm^{-3}, with the strain changing from 1% compressive to 1% tensile strain. For the corresponding cross-plane power factor $PF_{\perp}$ the optimal carrier concentration is about $N = 1 \times 10^{21}$ cm^{-3} at 1% compressive strain and increases by about a factor of 5 under the same strain conditions. For hole doping no evident change of the optimal doping could be found for varying strain, while the absolute value depends only weakly on the applied strain (cf figure 3(f)).

To summarize our findings, sections along the path of optimal electron doping are shown in figure 5. With this, it is obvious that even with optimized doping no enhancement by tensile or compressive [111]-strain can be obtained for the in-plane power factor $PF_{\parallel}$. For the cross-plane component $PF_{\perp}$, which is more relevant for possible SLs, an increase of the power factor of about 4% at 1% compressive strain was found. To obtain this rather small enhancement the electron charge carrier concentration has to be reduced by about a factor of 2.5 compared to the unstrained case.

3.3. Strained Si/Ge-SL on Si[111]

By introducing the concepts of carrier pocket engineering [15–17] and phonon–glass/electron–crystal [49, 50] to semiconducting SLs an enormous leap forward to maximize the thermoelectric FOM was proposed. Indeed, several proofs-of-principle showed a remarkable enhancement of the FOM for thermoelectric semiconducting heterostructures [7, 8, 17, 51]. With the thermal conductivity of SLs far below their alloy limit [52–55] and their constituents' bulk values, a main task in optimizing the FOM is to enhance or at least to retain advantageous electronic properties of the bulk materials, that is the power factor. For silicon-based SLs, carrier pocket engineering can be triggered by lattice strain. Using Si_{1-x}/Ge_x substrates in [111] and [100] orientations ZT values of 0.96 and 0.24, respectively, were predicted for strain-symmetrized[4] Si(20 Å)Ge(20 Å) SLs at room temperature. The latter case was experimentally confirmed with $ZT = 0.1$ at $N \approx 1 \times 10^{19}$ cm^{-3} [17], which is nevertheless about a sevenfold enhancement relative to bulk Si [13, 18]. These experimental findings encourage further research for strain-non-symmetrized Si(20 Å)/Ge(20 Å) SLs in [001]-orientation and Si(15 Å)/Ge(40 Å) SLs in [111]-orientation, with $ZT = 0.78$ and 1.25, respectively, predicted at $T = 300$ K [15].

While being in principle possible for very thin films [58, 59], to the best of our knowledge state-of-the-art thin film technology has not enabled strain-non-symmetrized SLs with satisfactory structural qualities and thicknesses for thermoelectric applications so far [56, 57, 60, 61]. Nevertheless, in the following the thermoelectric transport properties of a strain-non-symmetrized Si(5 Å)/Ge(5 Å) SL in [111]-orientation will be discussed, as the largest enhancement of the FOM is expected here [15].

The Si(5 Å)/Ge(5 Å) SL used is represented by a hexagonal six-atom unit cell (see the inset in figure 7(a)) with point group symmetry C_{3v} and a fixed in-plane lattice constant of $a = 5.434$ Å was used to simulate the bulk silicon substrate. Structural optimization of the atomic positions and the c-axis elongation of the unit cell was obtained using VASP [27]. The distinct interlayer distances δ in the [111]-direction were determined as $\delta_{Si_1-Si_2} = 2.359$ Å, $\delta_{Si_2-Si_3} = 0.784$ Å, $\delta_{Si_3-Ge_4} = 2.409$ Å, $\delta_{Ge_4-Ge_5} = 0.929$ Å, $\delta_{Ge_5-Ge_6} = 2.470$ Å, $\delta_{Ge_6-Si_1} = 0.851$ Å and are in good agreement with previous calculations [62]. The ratio $c/a = 2.551$ shows an increase of the lattice constant in the c-direction by about 4% compared to bulk Si. This is clearly dictated by the fixed in-plane Si lattice constant and the larger volume of Ge. Due to this, the Ge layer can be seen as compressively strained in the [111]-direction.

As has already been mentioned in the literature [62, 63], the face centred cubic (fcc) L high symmetry point in the [111] direction folds onto the hexagonal A high symmetry point at a c/a -ratio of 2.449. In addition, the fcc X point is equivalent to the hexagonal M point, while the symmetry directions fcc ΓX and hexagonal ΓM are inequivalent. This is due the fcc X point lying in an adjoining Brillouin zone. Under biaxial [111]-strain two inequivalent sets of the eight L points occur. There are two points along the c-axis in the [111] direction of growth which fold onto the A point and those in the six directions equivalent to $[11\bar{1}]$ hereafter denoted as L.

In figure 6 the band structure for the fully relaxed Si/Ge-SL in the hexagonal unit cell is shown. While in figure 6(a) the site-resolved bands for the Si/Ge-SL are depicted, in figure 6(b) the bands for pure Si on the fully relaxed Si/Ge positions are shown (blue dashed lines), as well as all sites occupied by Ge (red dotted lines) and the bands referring to the original Si/Ge-SL bands as shown in

[4] For an introduction to strain-symmetrized and strain-non-symmetrized Si/Ge superlattices we refer to the publications of Kasper *et al* [56, 57].

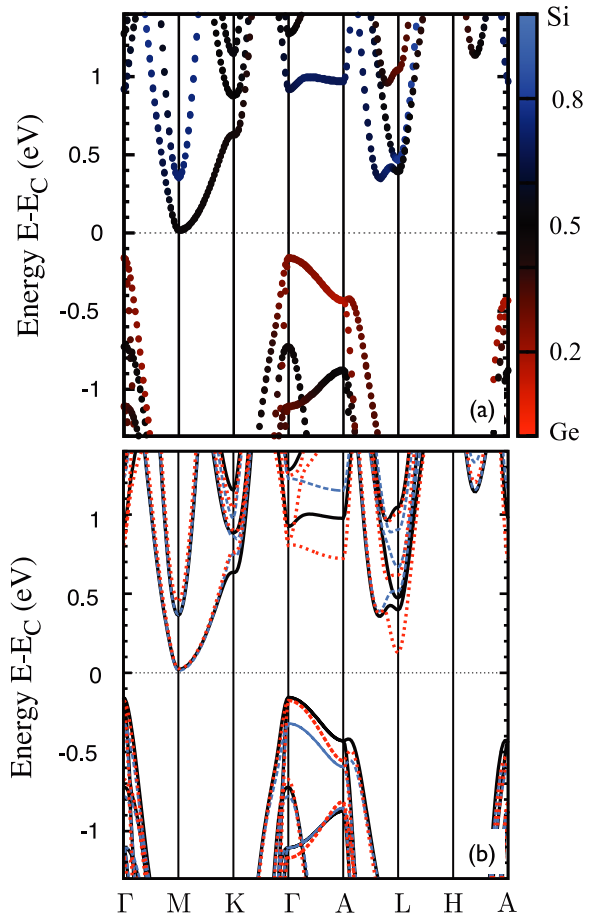

Figure 6. (a) The band structure of the Si/Ge-SL. The colour code of the bands refers to the atomic character of the bands. The red dots refer to the wavefunction character of pure germanium, while the blue dots refer to pure silicon like character. (b) The band structures of silicon (blue dashed lines), germanium (red dotted lines) and Si/Ge (black solid line). All three configurations are calculated in the lattice of Si/Ge. To allow comparison with (a), the bands are energetically matched at the CBM. The figure has not been corrected for the bandgap error.

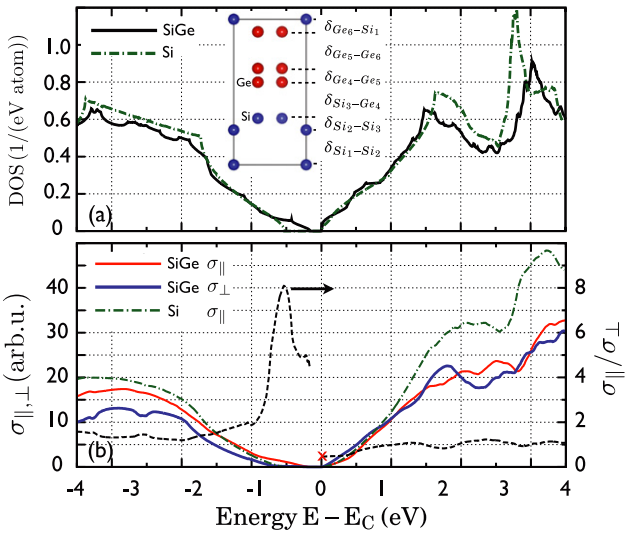

Figure 7. (a) The densities of states for bulk silicon (green dashed–dotted line) and the Si/Ge-SL (black solid line). As an inset the hexagonal unit cell of the Si/Ge-SL is shown [41]. Furthermore the interlayer distances are labelled, as referred to in the text. (b) The electrical conductivity in dependence on the position of the chemical potential μ at zero temperature, shown for bulk silicon (green dashed–dotted line) and the Si/Ge-SL in the in-plane (red solid line) and cross-plane (blue solid line) directions. The conductivity anisotropy (black dashed line referring to the right axis) is stated for the Si/Ge-SL. The cross at the CBM is the value obtained from an analytical effective mass approach.

figure 6(a) (black solid lines). Two main insights can be drawn. First, the VBM is located around the Γ point and has an almost pure Ge character, given by the red dots in figure 6(a). This is mainly due to the smaller bandgap of Ge and the accompanied band offset between Ge and Si. Furthermore, the compressive biaxial strain in the Ge layers decreases the gap size and favours a direct bandgap at Γ instead of an indirect one between Γ and L [64, 45, 65]. Valence bands of mixed Si/Ge character come into play around 0.65 eV below the CBM and suggest the local indirect Si bandgap between Γ and M to be almost retained bulk like. Second, the CBM is located at the M point and shows a strong mixing of Si and Ge character. Furthermore a strain-induced lifting of degeneracy occurs at the M point lowering a band of mixed character to the band edge and lifting a Si like band upwards in energy. As only the Ge layers in the SL are compressively strained while the Si layers are nearly unstrained, the Ge L-point CBM valleys split into A valleys located higher in energy and L valleys lower in energy [15, 65, 66]. These findings on the CBM and VBM characteristics are in agreement with experimental studies [59]. With this the uncorrected bandgap decreases to around 178 meV, which is about 30% of the uncorrected GGA gap for unstrained bulk Si. Furthermore, the effective masses at the CBM decrease to $M_1 = 0.125m_0$, $M_2 = 0.026m_0$ and $M_3 = 0.010m_0$.[5] Applying an effective mass approach [22] we find the conductivity anisotropy for energies near the CBM to be $\sigma_\parallel/\sigma_\perp = 0.6$, which clearly prefers cross-plane transport under electron doping.

The energy-dependent transport distribution functions in the in-plane and cross-plane directions and their ratio are displayed in figure 7(b) for the Si/Ge-SL and isotropic unstrained bulk Si. For the same systems the densities of states are shown in figure 7(a). As can be seen from figure 7(b) unfortunately the conductivity anisotropy near the valence band edge strongly increases to a value of 8 around 0.58 eV below the CBM, clearly suppressing cross-plane electronic transport under p-type doping. This behaviour is largely due to the localization of the Ge like VBM states, in space as well as energy. As can be deduced from figure 6(a) bands in the cross-plane direction (here ΓA) show pure Ge band character in an energy range of 0.18–0.74 eV below the CBM. Clearly, in this energy range cross-plane conduction is suppressed by states localized in the Ge layers and almost vanishing in the Si layers leading to a strongly increased conductivity anisotropy. At an energy of 0.38 eV below the CBM at Γ a light band with

[5] The corresponding eigenvectors were determined as $e_1 = (0.8, 0, 0.6)$, $e_2 = (0, 1, 0)$ and $e_3 = (0.6, 0, -0.8)$.

strong Si/Ge mixed character appears (cf the black solid line in figure 6(b)) leading to cross-plane transport through the Si and Ge layer forcing $\sigma_{\parallel}/\sigma_{\perp}$ to decrease, while saturating for values above 1, still indicating a preferred in-plane transport under hole doping.

In figures 8(a), (b) the doping-dependent thermopower and power factor for the Si/Ge-SL are shown, respectively. As a comparison the reference values for bulk silicon are stated as black dashed–dotted lines. We note that a temperature dependence of the energy gap was introduced by applying equation (2). For the Si/Ge-SL the[6] parameters are chosen as $U_{\mathrm{GGA}} = 0.78$ eV, $\alpha = 4.76 \times 10^{-4}$ eV K^{-1} and $\beta = 395$ K. However, in the highly degenerate limit ($N > 1 \times 10^{20}$ cm^{-3}) the temperature dependence of the gap plays a negligible role even for temperatures above 900 K.

From figure 8(a) it can be seen that the thermopower in the Si/Ge-SL under electron doping (blue lines in the lower panel) is comparable to that of bulk silicon and follows a Pisarenko relation [68]. Under hole doping (red lines in the upper panel) the thermopower is suppressed compared to bulk silicon by about 80 μV K^{-1} for $S_{\parallel}$ and $S_{\perp}$ in the relevant doping regime, which might be linked to a changed functional behaviour of the TDF $\mathcal{L}^{(0,1)}_{\perp,\parallel}(\mu, T)$. The latter can be deduced from figure 7(b) where apparent differences in the functional behaviour of $\sigma_{\perp,\parallel}$, which is proportional to $\mathcal{L}^{(0)}_{\perp,\parallel}(\mu, T)$, are visible especially in the valence bands of bulk Si and the Si/Ge-SL. The clear deviation of $S_{\perp}$ from the Pisarenko relation in the vicinity of $N \approx 3 \times 10^{21}$ cm^{-3} is related to the strongly increased conductivity anisotropy 0.58 eV below the VBM as shown in figure 7(b). Here, the strong suppression of $\sigma_{\perp}$ causes a larger $S_{\perp}$. Nevertheless, this slight enhancement of $S_{\perp}$ is not reflected in the power factor of the p-type Si/Ge-SL. As shown in figure 8(b) $S_{\parallel}$ and $S_{\perp}$ are always smaller than the values for bulk Si under hole doping (red lines). Obviously, the suppressed electrical conductivity, especially in the cross-plane direction, is responsible for this result. A power factor of about 9 μW cm^{-1} K^{-2} is found for $\mathrm{PF}_{\parallel}$ at $N \approx 3 \times 10^{20}$ cm^{-3}, while in the cross-plane direction the same value can be stated at huge values of $N \approx 3 \times 10^{21}$ cm^{-3}, clearly evoked by the anomaly in the thermopower. More interesting is the case of electron doping (blue lines in figure 8(a)). With the thermopower's behaviour almost bulk like and conductivity anisotropies $\sigma_{\parallel}/\sigma_{\perp}$ below 1 an enhanced power factor in the required cross-plane direction is found. Compared to bulk silicon the $\mathrm{PF}_{\perp}$ is enhanced by 10% and reaches a value of 60 μW cm^{-1} K^{-2} at an electron concentration of $N \approx 7 \times 10^{20}$ cm^{-3}. With that the optimal charge carrier concentration is four times smaller compared to bulk Si. For the in-plane component $\mathrm{PF}_{\parallel}$ almost no reduction can be seen, while the maximal value of 53 μW cm^{-1} K^{-2} is shifted to slightly larger charge carrier concentrations.

3.4. Towards the figure of merit

In figure 9(a) the FOM in the cross-plane direction for the Si/Ge-SL (blue lines) and the more promising electron-doped case is shown. Different temperatures are chosen to demonstrate the evaluation of maximal ZT and the range of optimal charge carrier concentration. As a comparison the FOM for bulk Si is shown as a black dashed–dotted

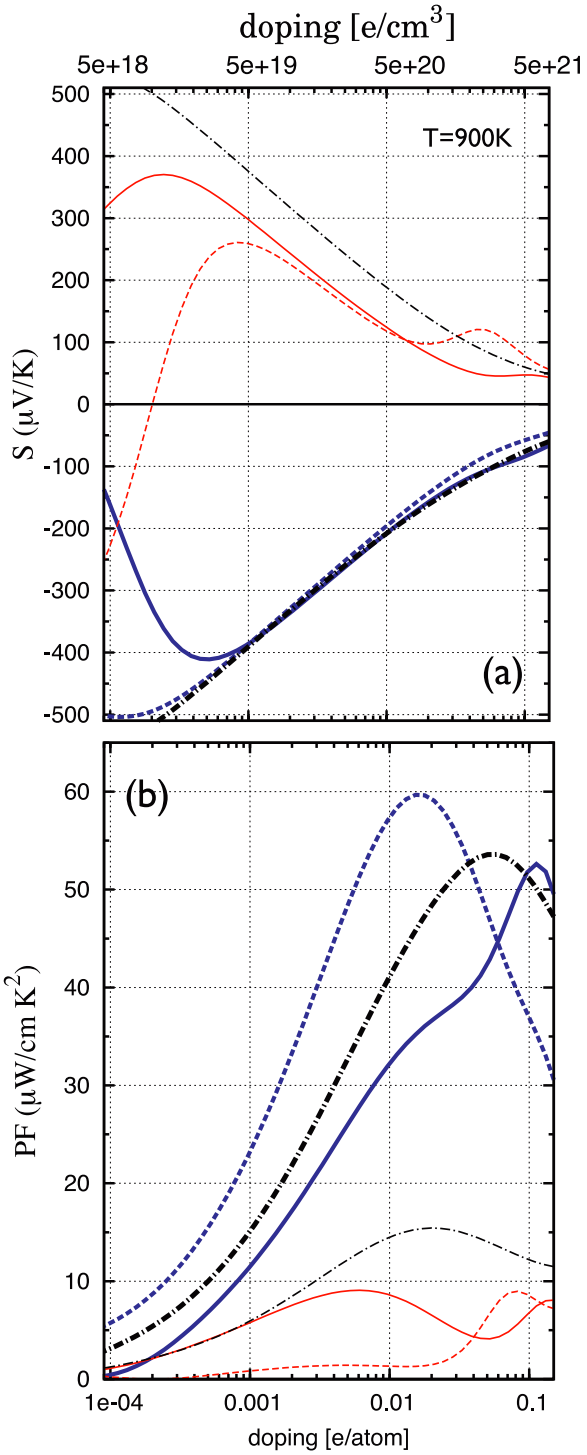

Figure 8. (a) The in-plane (solid lines) and cross-plane (dashed lines) doping-dependent thermopowers at 900 K for the Si/Ge-SL under electron (thick blue lines) and hole doping (thin red lines). For comparison the values for bulk silicon are given (black dashed–dotted lines). (b) The in-plane (solid lines) and cross-plane (dashed lines) doping-dependent power factors at 900 K for the Si/Ge-SL under electron (thick blue lines) and hole doping (thin red lines). Again, for comparison the values for bulk silicon are given (black dashed–dotted lines).

[6] Here we adapted experimental data for $Si_{0.5}Ge_{0.5}$ alloys from [67].

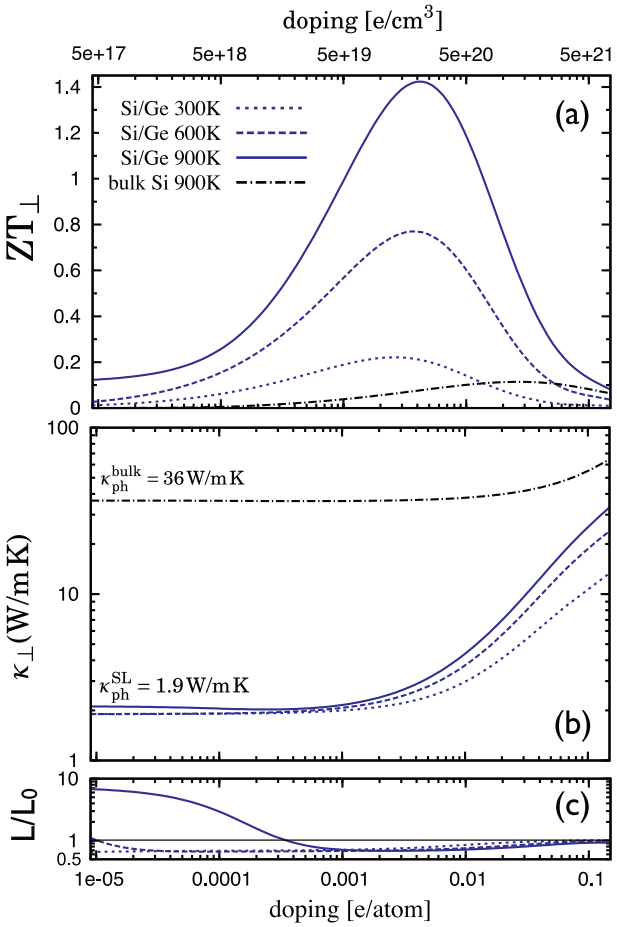

Figure 9. (a) The doping-dependent cross-plane figures of merit $ZT_\perp$ of the Si/Ge-SL (blue lines) and bulk Si (black lines) under electron doping at different temperatures. (b) The total thermal conductivities $\kappa_\perp$ in the cross-plane direction for the Si/Ge-SL (blue lines) and bulk Si (black lines) under electron doping at different temperatures. While the electronic part $\kappa_{el\perp}$ was calculated, the lattice part $\kappa_{ph\perp}$ was estimated from experiments [13, 55] and is constant for varying charge carrier concentration. (c) The calculated cross-plane Lorenz function $L_\perp = \kappa_{el\perp}(\sigma_\perp T)^{-1}$ is related to the metallic limit $L_0 = 2.44 \times 10^{-8}$ W Ω K^{-2}.

line too. To present results for the FOM, knowledge of the thermal conductivity is relevant. For this purpose, the electronic part of the thermal conductivity $\kappa_{el\perp}$ was calculated applying equation (6), while the lattice part $\kappa_{ph\perp}$ was taken from experiment. Here, $\kappa_{ph\perp} = 36$ W m^{-1} K^{-1} [13] was used for bulk Si at 900 K, while $\kappa_{ph\perp} = 1.9$ W m^{-1} K^{-1} was used for the Si/Ge-SL [55], with the latter being rather optimistic, since it is smaller than the expected nano-alloy limit of 2.5 W m^{-1} K^{-1} [69], but achievable in Si/Ge-SL [53, 55, 70]. However, from figure 9(b) one can deduce that for thermoelectric reliable charge carrier concentrations above 4×10^{20} cm^{-3} the electronic contribution to the total thermal conductivity dominates over its lattice part. At 900 K for $N \approx 1.5 \times 10^{20}$ cm^{-3} the electronic part amounts to 0.73 W m^{-1} K^{-1}, clearly smaller than the lattice part. This contribution increases significantly at higher temperatures and charge carrier concentrations omitting higher absolute values of the FOM. However, $ZT_\perp$ above unity can be reached for operating temperatures higher than 750 K and electron-doping $N \approx 1.5$–3×10^{20} cm^{-3}.

At room temperature a $ZT_\perp \approx 0.2$ is achieved in a broad doping range of $N \approx 5$–25×10^{19} cm^{-3}. Although this value is an order of magnitude higher than the bulk Si value of $ZT \approx 0.01$ [13, 15, 18], it is still less than the postulated values of $ZT_\perp = 0.96$ and $ZT_\perp = 1.25$ by Koga *et al* [15] for strain-symmetrized and strain-non-symmetrized Si/Ge-SL, respectively. With these values, and using a rather conservative value of $\kappa_{ph\perp} = 7.3$ W m^{-1} K^{-1} for their estimations, they expect enormous power factors of $PF_\perp \approx 250$ μW cm^{-1} K^{-2} and $PF_\perp \approx 340$ μW cm^{-1} K^{-2} for the strain-optimized Si/Ge-SL in the [111]-direction. We found $PF_\perp \approx 15$ μW cm^{-1} K^{-2} at 300 K and $N \approx 1 \times 10^{20}$ cm^{-3} for the Si/Ge-SL. Even though a convergence of carrier pockets is not fully achieved in our superlattice, power factors beyond 200 μW cm^{-1} K^{-2} seem to be very high, as state-of-the-art power factors near or above room temperature are well below 100 μW cm^{-1} K^{-2} [7, 71, 72]. A benefit from thermionic emission even at moderate temperatures cannot be expected in Si/Ge-SL [73–75]. We note that at very low temperatures below 10 K huge PFs of about 100–1000 μW cm^{-1} K^{-2} were reported for bulk Fe_2Sb_2 and $ZnO_{1-x}Se_x$ [76, 77].

As an addition, in figure 9(c) the doping-dependent Lorenz function $L_\perp = \kappa_{el\perp}(\sigma_\perp T)^{-1}$ as defined via equations (5) and (6) is presented. From figure 9(c) it is obvious that the Lorenz number $L_\perp$ can be substantially different from the metallic limit L_0. Nevertheless, for very large charge carrier concentrations and the chemical potential located deep inside the conduction band, $L_\perp$ almost coincides with L_0. At intermediate and thermoelectrically relevant charge carrier concentrations of $N \approx 5$–50×10^{19} cm^{-3} $L_\perp$ can be much smaller than L_0. For 900 K and $N \approx 1.25 \times 10^{20}$ cm^{-3} we find a minimal value of $L_\perp \approx 0.7L_0$. At smaller charge carrier concentrations $L_\perp$ rapidly increases and reaches $L_\perp \approx 7L_0$ for electron charge carrier concentrations of $N < 1 \times 10^{18}$ cm^{-3} in the intrinsic doping regime. At decreasing temperatures minimal values of the Lorenz function are obtained at much smaller charge carrier concentrations. Furthermore, the maximal values of L shift to smaller charge carrier concentrations too, and can reach huge values of L at very low temperatures and charge carrier concentrations. The effect, which is responsible for the suppression of the Lorenz function to values below the metallic limit L_0, is termed the bipolar thermodiffusion effect [78–80] and is maximized for positions of the chemical potential near the band edges. However, a Lorenz function $L \neq L_0$ can have consequences for the determination of the thermal conductivity. The Lorenz factor is generally used to separate κ_{el} and κ_{ph}. At thermoelectrically advisable charge carrier concentrations applying the metallic value L_0 to determine the lattice thermal conductivity could lead to an overestimation of the electronic thermal conductivity, and consequently to an underestimation of the lattice contribution.

4. Conclusions and outlook

With the presented results we have shown, that strain in the [111]-direction is not sufficient to significantly enhance the thermoelectric transport properties in bulk Si for energy harvesting applications. In the low-temperature and low-doping case large enhancements were found under tensile strain for $PF_{\parallel}$ (electron doping) and $PF_{\perp}$ (hole doping) and under compressive strain for $PF_{\perp}$ (electron doping). This could have a negative impact for metal–oxide–semiconductor devices involving [111]-strained Si. Here, in the low-temperature and low-doping regime, small temperature gradients in the devices could lead to an additional parasitic electrical power, which could be far larger than expected from unstrained bulk.

The enhancements found in the high-temperature and high-doping regime were distinctly smaller. Here slight enhancements of 5% for $PF_{\perp}$ were found under compressive strain. It is more interesting that the power factor is robust against [111]-strain, especially under hole doping. Thus, thermoelectric SLs based on [111]-strained Si could provide an enhanced FOM, as κ_{ph} is most likely reduced in SLs. We note that due to the high bulk thermal conductivity and the only modest gain in the power factor by [111]-strain engineering, bulk silicon remains an unfavourable thermoelectric, even if the electronic transport properties are strain optimized. However, from comparison with earlier studies on biaxially [001]-strained silicon [18], we confirm that strain in the [111]-direction, e.g. in silicon-based SLs, should be preferred, as the carrier pocket degeneracy is retained and therefore the thermopower and power factor can be maximized.

To deal with this, we investigated the anisotropic thermoelectric transport of a [111]-oriented Si/Ge superlattice. At a first glance we have shown that no degradation of the electronic transport by the heterostructure is expected for electron doping, while even showing an enhancement of 10% in $PF_{\perp}$ compared to bulk Si. Assuming a decrease in lattice thermal conductivity large enhancements in *ZT* to 0.2 and 1.4 are achieved at 300 K and 900 K, respectively. Under hole doping the electronic transport in the Si/Ge-SL is heavily suppressed due to quantum-well effects. Here the cross-plane power factor $PF_{\perp}$ is expected to show only around 50% of the bulk maximal value, leading to small *ZT* values.

Acknowledgments

This work was supported by the Deutsche Forschungsgemeinschaft, SPP 1386 ‘Nanostrukturierte Thermoelektrika: Theorie, Modellsysteme und kontrollierte Synthese’. N F Hinsche is a member of the International Max Planck Research School for Science and Technology of Nanostructures.

References

[1] Seebeck T J 1826 Über die magnetische Polarisation der Metalle und Erze durch Temperatur-Differenz *Ann. Phys., Lpz.* **82** 253–86

[2] Ioffe A F 1958 The revival of thermoelectricity *Sci. Am.* **199** 31–7

[3] Majumdar A 2004 Thermoelectricity in semiconductor nanostructures *Science* **303** 777

[4] Böttner H, Chen G and Venkatasubramanian R 2006 Aspects of thin-film superlattice thermoelectric materials, devices, and applications *MRS Bull.* **31** 211

[5] Tritt T M and Subramanian M A 2006 Thermoelectric materials, phenomena, and applications: a bird’s eye view *MRS Bull.* **31** 188–98

[6] Sales B C 2002 Thermoelectric materials: smaller is cooler *Science* **295** 1248

[7] Venkatasubramanian R, Siivola E and Colpitts T 2001 Thin-film thermoelectric devices with high room-temperature figures of merit *Nature* **413** 597

[8] Harman T, Taylor P, Walsh M and LaForge B 2002 Quantum dot superlattice thermoelectric materials and devices *Science* **297** 2229

[9] Dresselhaus M, Chen G, Tang M and Yang R 2007 New directions for low-dimensional thermoelectric materials *Adv. Mater.* **19** 1

[10] Vining C B 2008 Materials science: desperately seeking silicon *Nature* **451** 132–3

[11] Hochbaum A, Chen R, Delgado R and Liang W 2008 Enhanced thermoelectric performance of rough silicon nanowires *Nature* **451** 163

[12] Boukai A I, Bunimovich Y, Tahir-Kheli J, Yu J K, Goddard Iii W A and Heath J R 2008 Silicon nanowires as efficient thermoelectric materials *Nature* **451** 168–71

[13] Bux S K, Blair R G, Gogna P K, Lee H, Chen G, Dresselhaus M S, Kaner R B and Fleurial J-P 2009 Nanostructured bulk silicon as an effective thermoelectric material *Adv. Funct. Mater.* **19** 2445–52

[14] Tang J, Wang H T, Lee D H, Fardy M, Huo Z, Russell T P and Yang P 2010 Holey silicon as an efficient thermoelectric material *Nano Lett.* **10** 4279

[15] Koga T, Sun X, Cronin S B and Dresselhaus M S 1999 Carrier pocket engineering applied to strained Si/Ge superlattices to design useful thermoelectric materials *Appl. Phys. Lett.* **75** 2438

[16] Koga T, Harman T, Cronin S and Dresselhaus M 1999 Mechanism of the enhanced thermoelectric power in (111)-oriented n-type PbTe/$Pb_{1-x}Eu_xTe$ multiple quantum wells *Phys. Rev.* B **60** 14286

[17] Koga T, Cronin S, Dresselhaus M and Liu J 2000 Experimental proof-of-principle investigation of enhanced *ZT* in (001) oriented Si/Ge superlattices *Appl. Phys. Lett.* **77** 1490

[18] Hinsche N, Mertig I and Zahn P 2011 Effect of strain on the thermoelectric properties of silicon: an *ab initio* study *J. Phys.: Condens. Matter* **23** 295502

[19] Giannozzi P *et al* 2009 Quantum espresso: a modular and open-source software project for quantum simulations of materials *J. Phys.: Condens. Matter* **21** 395502

[20] Mertig I 1999 Transport properties of dilute alloys *Rep. Prog. Phys.* **62** 237–76

[21] Hinsche N, Yavorsky B, Mertig I and Zahn P 2011 Influence of strain on anisotropic thermoelectric transport in Bi_2Te_3 and Sb_2Te_3 *Phys. Rev.* B **84** 165214

[22] Zahn P, Hinsche N, Yavorsky B and Mertig I 2011 Bi_2Te_3: implications of the rhombohedral *k*-space texture on the evaluation of the in-plane/out-of-plane conductivity anisotropy *J. Phys.: Condens. Matter* **23** 505504

[23] Perdew J P, Burke K and Ernzerhof M 1996 Generalized gradient approximation made simple *Phys. Rev. Lett.* **77** 3865–8

[24] Corso A and Conte A 2005 Spin–orbit coupling with ultrasoft pseudopotentials: application to Au and Pt *Phys. Rev.* B **71** 115106

[25] Yu D, Zhang Y and Liu F 2008 First-principles study of electronic properties of biaxially strained silicon: effects on charge carrier mobility *Phys. Rev.* B **78** 245204

[26] Bouhassoune M and Schindlmayr A 2009 Electronic structure and effective masses in strained silicon *Phys. Status Solidi* c **7** 460–3

[27] Kresse G and Furthmüller J 1996 Efficient iterative schemes for *ab initio* total-energy calculations using a plane-wave basis set *Phys. Rev.* B **54** 11169

[28] Godby R W, Schlüter M and Sham L J 1988 Self-energy operators and exchange–correlation potentials in semiconductors *Phys. Rev.* B **37** 10159–75

[29] Varshni Y P 1967 Temperature dependence of the energy gap in semiconductors *Physica* **34** 149–54

[30] Vojta T, Mertig I and Zeller R 1992 Calculation of the residual resistivity and the thermoelectric power of sp impurities in silver *Phys. Rev.* B **46** 16761

[31] Thonhauser T, Scheidemantel T J and Sofo J O 2004 Improved thermoelectric devices using bismuth alloys *Appl. Phys. Lett.* **85** 588

[32] Singh D J 2010 Doping-dependent thermopower of PbTe from Boltzmann transport calculations *Phys. Rev.* B **81** 195217

[33] Scheidemantel T J, Ambrosch-Draxl C, Thonhauser T, Badding J V and Sofo J O 2003 Transport coefficients from first-principles calculations *Phys. Rev.* B **68** 125210

[34] Jacoboni C, Canali C, Ottaviani G and Quaranta A A 1977 A review of some charge transport properties of silicon *Solid-State Electron.* **20** 77–89

[35] Dziekan T, Zahn P, Meded V and Mirbt S 2007 Theoretical calculations of mobility enhancement in strained silicon *Phys. Rev.* B **75** 195213

[36] Roldán J B, Gámiz F, LópezVillanueva J A and Carceller J E 1996 A Monte Carlo study on the electron transport properties of high performance strained Si on relaxed $Si_{1-x}Ge_x$ channel MOSFETs *J. Appl. Phys.* **80** 5121

[37] Mahan G and Sofo J O 1996 The best thermoelectric *Proc. Natl Acad. Sci.* **93** 7436

[38] Lehmann G and Taut M 1972 On the numerical calculation of the density of states and related properties *Phys. Status Solidi* b **54** 469–77

[39] Zahn P, Mertig I, Richter M and Eschrig H 1995 *Ab initio* calculations of the giant magnetoresistance *Phys. Rev. Lett.* **75** 2996–9

[40] Mertig I, Mrosan E and Ziesche P 1987 *Multiple Scattering Theory of Point Defects in Metals: Electronic Properties* (Leipzig: B G Teubner)

[41] Momma K and Izumi F 2011 VESTA3 for three-dimensional visualization of crystal, volumetric and morphology data *J. Appl. Crystallogr.* **44** 1272–6

[42] Baykan M O, Thompson S E and Nishida T 2010 Strain effects on three-dimensional, two-dimensional, and one-dimensional silicon logic devices: predicting the future of strained silicon *J. Appl. Phys.* **108** 093716

[43] Sun G, Sun Y, Nishida T and Thompson S E 2007 Hole mobility in silicon inversion layers: stress and surface orientation *J. Appl. Phys.* **102** 084501

[44] Boykin T, Kharche N and Klimeck G 2007 Brillouin-zone unfolding of perfect supercells having nonequivalent primitive cells illustrated with a SiGe tight-binding parameterization *Phys. Rev.* B **76** 035310

[45] Niquet Y, Rideau D, Tavernier C, Jaouen H and Blase X 2009 Onsite matrix elements of the tight-binding Hamiltonian of a strained crystal: application to silicon, germanium, and their alloys *Phys. Rev.* B **79** 245201

[46] Park M S, Song J-H, Medvedeva J E, Kim M, Kim I G and Freeman A J 2010 Electronic structure and volume effect on thermoelectric transport in p-type Bi and Sb tellurides *Phys. Rev.* B **81** 155211

[47] Thompson S E, Sun G, Choi Y S and Nishida T 2006 Uniaxial-process-induced strained-Si: extending the CMOS roadmap *IEEE Trans. Electron Devices* **53** 1010–20

[48] Pei Y, Shi X, LaLonde A, Wang H, Chen L and Jeffrey Snyder G 2011 Convergence of electronic bands for high performance bulk thermoelectrics *Nature* **473** 66–9

[49] Slack G A 1995 *CRC Handbook of Thermoelectrics* (Boca Raton, FL: CRC Press) chapter 34, p 407

[50] Poudel B, Hao Q, Ma Y, Lan Y, Minnich A, Yu B, Yan X, Wang D, Muto A and Vashaee D 2008 High-thermoelectric performance of nanostructured bismuth antimony telluride bulk alloys *Science* **320** 634

[51] Hicks L, Harman T, Sun X and Dresselhaus M 1996 Experimental study of the effect of quantum-well structures on the thermoelectric figure of merit *Phys. Rev.* B **53** R10493

[52] Venkatasubramanian R 2000 Lattice thermal conductivity reduction and phonon localizationlike behavior in superlattice structures *Phys. Rev.* B **61** 3091–7

[53] Borca-Tasciuc T 2000 Thermal conductivity of symmetrically strained Si/Ge superlattices *Superlattices Microstruct.* **28** 199–206

[54] Chakraborty S, Kleint C A, Heinrich A, Schneider C M, Schumann J, Falke M and Teichert S 2003 Thermal conductivity in strain symmetrized Si/Ge superlattices on Si(111) *Appl. Phys. Lett.* **83** 4184

[55] Lee S, Cahill D and Venkatasubramanian R 1997 Thermal conductivity of Si–Ge superlattices *Appl. Phys. Lett.* **70** 2957

[56] Kasper E, Kibbel H, Jorke H, Brugger H, Friess E and Abstreiter G 1988 Symmetrically strained Si/Ge superlattices on Si substrates *Phys. Rev.* B **38** 3599–601

[57] Kasper E 1986 Growth and properties of Si/SiGe superlattices *Surf. Sci.* **174** 630–9

[58] Pearsall T, Bevk J, Feldman L, Bonar J, Mannaerts J and Ourmazd A 1987 Structurally induced optical transitions in Ge–Si superlattices *Phys. Rev. Lett.* **58** 729–32

[59] Pearsall T, Bevk J, Bean J, Bonar J, Mannaerts J and Ourmazd A 1989 Electronic structure of Ge/Si monolayer strained-layer superlattices *Phys. Rev.* B **39** 3741–57

[60] Brunner K 2002 Si/Ge nanostructures *Rep. Prog. Phys.* **65** 27

[61] Kuan T S and Iyer S S 1991 Strain relaxation and ordering in SiGe layers grown on (100), (111), and (110) Si surfaces by molecular-beam epitaxy *Appl. Phys. Lett.* **59** 2242

[62] Bass J M and Matthai C C 1990 Electronic structure of (111) Si/Ge superlattices *J. Phys.: Condens. Matter* **2** 7841

[63] Salehpour M R and Satpathy S 1990 Comparison of electron bands of hexagonal and cubic diamond *Phys. Rev.* B **41** 3048

[64] Tahini H, Chroneos A, Grimes R W, Schwingenschlögl U and Dimoulas A 2012 Strain-induced changes to the electronic structure of germanium *J. Phys.: Condens. Matter* **24** 195802

[65] Zhang F, Crespi V and Zhang P 2009 Prediction that uniaxial tension along 111 produces a direct band gap in germanium *Phys. Rev. Lett.* **102** 156401

[66] Rideau D, Feraille M, Ciampolini L, Minondo M, Tavernier C, Jaouen H and Ghetti A 2006 Strained Si, Ge, and $Si_{1-x}Ge_x$ alloys modeled with a first-principles-optimized full-zone kp method *Phys. Rev.* B **74** 195208

[67] Braunstein R, Moore A R and Herman F 1958 Intrinsic optical absorption in germanium–silicon alloys *Phys. Rev.* **109** 695–710

[68] Ioffe A F 1960 *Physics of Semiconductors* (New York: Academic)

[69] Wang X W, Lee H, Lan Y C, Zhu G H, Joshi G, Wang D Z, Yang J, Muto A J, Tang M Y and Klatsky J 2008 Enhanced thermoelectric figure of merit in nanostructured n-type silicon germanium bulk alloy *Appl. Phys. Lett.* **93** 193121

[70] Pernot G, Stoffel M, Savic I, Pezzoli F, Chen P, Savelli G, Jacquot A, Schumann J, Denker U and Mönch I 2010 Precise control of thermal conductivity at the nanoscale through individual phonon-scattering barriers *Nature Mater.* **9** 491

[71] Jalan B and Stemmer S 2010 Large seebeck coefficients and thermoelectric power factor of La-doped $SrTiO_3$ thin films *Appl. Phys. Lett.* **97** 3

[72] Okinaka N and Akiyama T 2006 Latent property of defect-controlled metal oxide: nonstoichiometric titanium oxides as prospective material for high-temperature thermoelectric conversion *Japan. J. Appl. Phys.* **45** 7009–10

[73] Vashaee D and Shakouri A 2007 Thermionic power generation at high temperatures using SiGe/Si superlattices *J. Appl. Phys.* **101** 053719

[74] Shakouri A and Bowers J E 1997 Heterostructure integrated thermionic coolers *Appl. Phys. Lett.* **71** 1234

[75] Vashaee D and Shakouri A 2004 Improved thermoelectric power factor in metal-based superlattices *Phys. Rev. Lett.* **92** 106103

[76] Sun P, Oeschler N, Johnsen S, Iversen B B and Steglich F 2009 Huge thermoelectric power factor: $FeSb_2$ versus $FeAs_2$ and $RuSb_2$ *Appl. Phys. Express* **2** 091102

[77] Lee J-H, Wu J and Grossman J C 2010 Enhancing the thermoelectric power factor with highly mismatched isoelectronic doping *Phys. Rev. Lett.* **104** 016602

[78] Nolas G S and Goldsmid H J 2004 *Thermal Conductivity: Theory, Properties, and Applications* (New York: Kluwer Academic) chapter 1.4, p 110

[79] Chaput L, Pécheur P, Tobola J and Scherrer H 2005 Transport in doped skutterudites: *ab initio* electronic structure calculations *Phys. Rev.* B **72** 085126

[80] Flage-Larsen E and Prytz O 2011 The Lorenz function: its properties at optimum thermoelectric figure-of-merit *Appl. Phys. Lett.* **99** 202108